Thermal Convection in a Rotating Fluid Annulus: Part 2. Classes of Axisymmetric Flow

GARETH P. WILLIAMS

Geophysical Fluid Dynamics Laboratory, ESSA, Washington, D. C.

(Manuscript received 23 September 1966)

ABSTRACT

This paper presents the solutions obtained for various axisymmetric thermal convection flows in a rotating annulus. Initially, a solution is obtained for a flow whose interior structure has been observed in detail. A comparison reveals the similarity of the experimental and computed temperature fields and shows the discrepancy to be independent of the computational resolution. On increasing the resolution, the Nusselt number decreases and converges to a value close to that observed. For this particular flow the rotation rate is zero and the flow consists of a direct meridional cell with a large stagnant interior. The associated isotherms lie horizontally in the interior such that the vertical temperature gradient is constant.

Secondly, we present solutions of five flows with a rigid surface. These flows cover a wide range of values of the external driving parameters so that physical processes vary from predominately viscous and conduction diffusion to free convection transports. Despite these differences, all five flows exhibit a similar structure, i.e., the interior flows form direct (Hadley) cells with sidewall countercurrents and the zonal flow reverses sign near the center of the fluid. Interpolation of the Nusselt number values yields a $(\Delta T/\Omega)^{0.5}$ dependency. Compared to the Ω^{-1} dependency of free surface flows, the rigid surface system forms the better transporting mechanism and is less inhibited by rotation.

1. Introduction

This paper forms the second part of a study of axisymmetric thermal convection of a fluid contained in a rotating annulus. In the experiments, water is contained between two coaxial cylinders which rotate about their axis. The cylinder walls are held at constant temperature and for particular rotation rates symmetrical flow about the axis of rotation results; such flows will be examined by obtaining numerical solutions of the Navier-Stokes equations. In contrast to the flows considered in Part 1, solutions will be obtained for a series of flows which have a rigid surface. The presence of this lid makes the physical system more symmetrical.

The purpose of this paper is to examine the possible species of axisymmetric flow, and the accuracy of the numerical technique employed. For the latter purpose, the equations are solved for a flow which has been examined experimentally by Bowden and Eden (1965).

In certain instances, some axisymmetric flows may be determined mainly by frictional forces and heat conduction (as in the so-called lower symmetric regime), whereas in other cases, flows tend to be more convectively determined (as in the upper symmetric regime). To examine the flows under these various types of physical processes, the 5 flows taken cover a wide range of values in the Rossby-Taylor diagram. Axisymmetric flow can occur for numerous parameter combinations. In this study, only the rotation rate and temperature differential are varied; the geometry and physical constants remain unaltered throughout.

2. A comparative experiment

A solution was made for a flow, A1 of Table 1, for which observational evidence exists. Starting from a typical initial state, described in Part 1, integrations with grids of 11, 21 and 41 points in each direction produced steady state flows whose integrals are shown in Fig. 1. These integrals appear to converge to values approximately equal to those given by the 41 grid point scheme. The values of $E_k:E_p=0.9497$, $\epsilon_k=0.9406$ and $\epsilon_p=-0.9319$ indicate the degree of steadiness, for they are within 1 per cent of balancing. The fluid takes approximately the same length of real time, 10 min, to achieve steadiness for all grid systems.

Similarly balanced are the Nusselt numbers of the inner cylinder, $\mathrm{Nu}(a)=6.3273$, and the outer cylinder $\mathrm{Nu}(b)=6.3739$, with a trend value of 6.35 indicated for their mean, $\mathrm{N\bar{u}}$. These values fall short of the estimates of $\mathrm{N\bar{u}}$ given by the 11 and 21 grid point solutions. The experimental data of Bowden and Eden (1965) provides an estimate of the actual Nusselt number for flow A1. Allowing for a slight difference in the width between cylinders, $b-a$, the fluid depth d, temperature differential ΔT, and for a possible 5 per cent systematic error in observation, the experimental Nusselt number lies within the range of 6.7 ± 0.4. This value agrees with the calculated one.

The close similarity between the detailed structure of the temperature contours of computation and observation may be seen from Fig. 2. The observations were made for 3 positions, i.e., at the center and 0.65 cm on either side of it, at heights of $z=0, 1, 2, \cdots 10$ cm,

TABLE 1. Structure of cases computed. Cases A3 and B2 are discussed in Part 1.

Case	Physical system	Surface condition	Number of grid intervals in r, z	ΔT (°C)	Ω (rad sec^{-1})	π_4	π_5
A1	BE	Fixed	40×40	6.0	0.000	—	—
A2	FH	Fixed	40×60	9.0	0.700	2.863	4.079×10^{5}
A3	FH	Free	40×80	29.0	1.342	2.510	1.500×10^{6}
B1	FH	Fixed	40×40	2.3	1.100	0.296	1.010×10^{6}
B2	FH	Free	40×80	29.0	2.125	1.001	3.759×10^{6}
C1	FH	Fixed	40×40	1.2	0.500	0.748	2.080×10^{5}
C2	FH	Fixed	40×40	0.1	0.350	0.127	1.020×10^{5}
D1	FH	Fixed	40×40	0.2	1.100	0.026	1.010×10^{6}

System BE: $a=3$ cm, $b=5$ cm, $d=10$ cm, $\nu=0.941\times10^{-2}$ cm^{-2} sec^{-1}, $\kappa=1.420\times10^{-3}$ cm^{2} sec, $\beta=2.380\times10^{-4}$ (°C)$^{-1}$, $\bar{T}=23$C, $\pi_6=6.58$.

System FH: $a=3.48$ cm, $b=6.02$ cm, $d=5$ cm, $\nu=1.008\times10^{-2}$ sec^{-1}, $\kappa=1.420\times10^{-3}$ cm^{2} sec, $\beta=2.050\times10^{-4}$ (°C)$^{-1}$, $\bar{T}=20$C, $\pi_6=7.19$.

so that we can only regard the observed field as being a smoothed, interpolated interpretation of the true temperature field. The observed isotherms do not contain horizontal sections as do the computed contours; in general, they appear to slope up toward the outer cylinder. However, if the interior computed field is smoothed in the same way as the observations have been, then there is a general agreement between the two. If we divide the height into 8 levels, the corresponding isotherms all lie within corresponding sections. This is more clearly illustrated in Fig. 3, where the temperature is graphed as a function of height for the central plane $r=(a+b)/2$. The temperature converges toward the 41 grid point solution and the disagreement with the observed field is independent of resolution.

Flow structure. Fig. 4 contains the details of the steady state flow field of case A1. The flow takes place in the vertical plane only and is confined to narrow regions at the extremities of the fluid. The fluid exhibits strong upward and downward flow at the outer (hot) and inner (cold) cylinders, respectively, but the cross flows are not so intense. There appears to be little or no motion within the central core of the fluid. Although the fields possess a degree of symmetry, the maximum

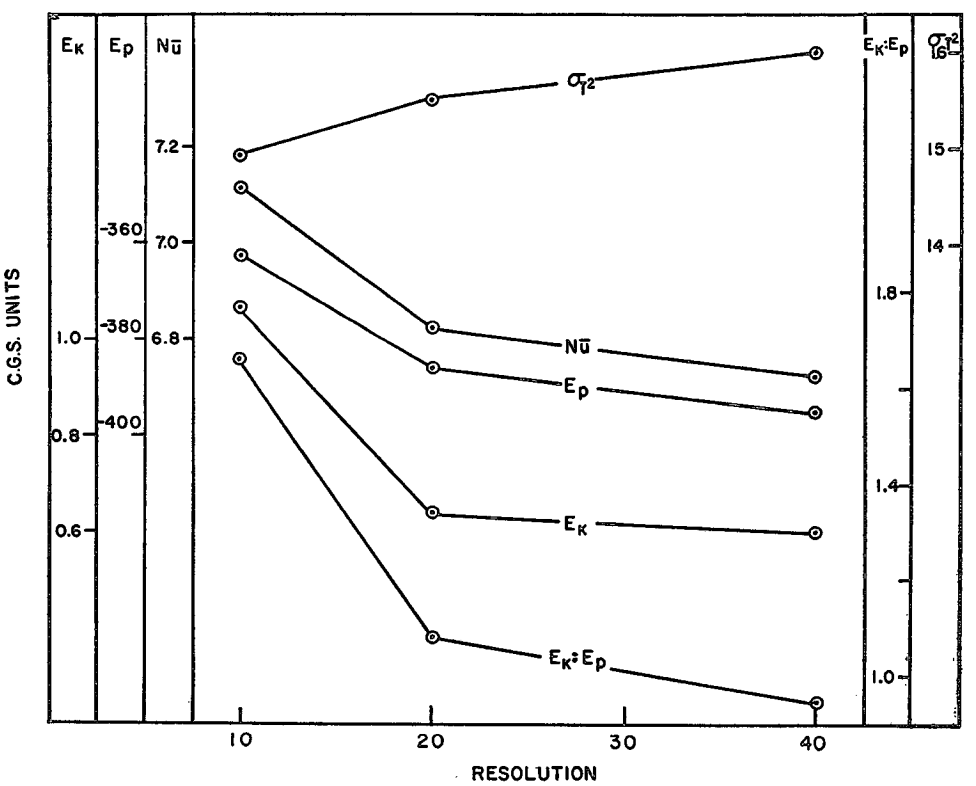

FIG. 1. Steady state integrals, derived from solutions which were obtained with 10, 20 and 40 grid spaces in each dimension, demonstrate the convergence of the solutions with increasing resolution for flow A1 ($\Omega=0$). For an explanation of the integral notation refer to Part 1.

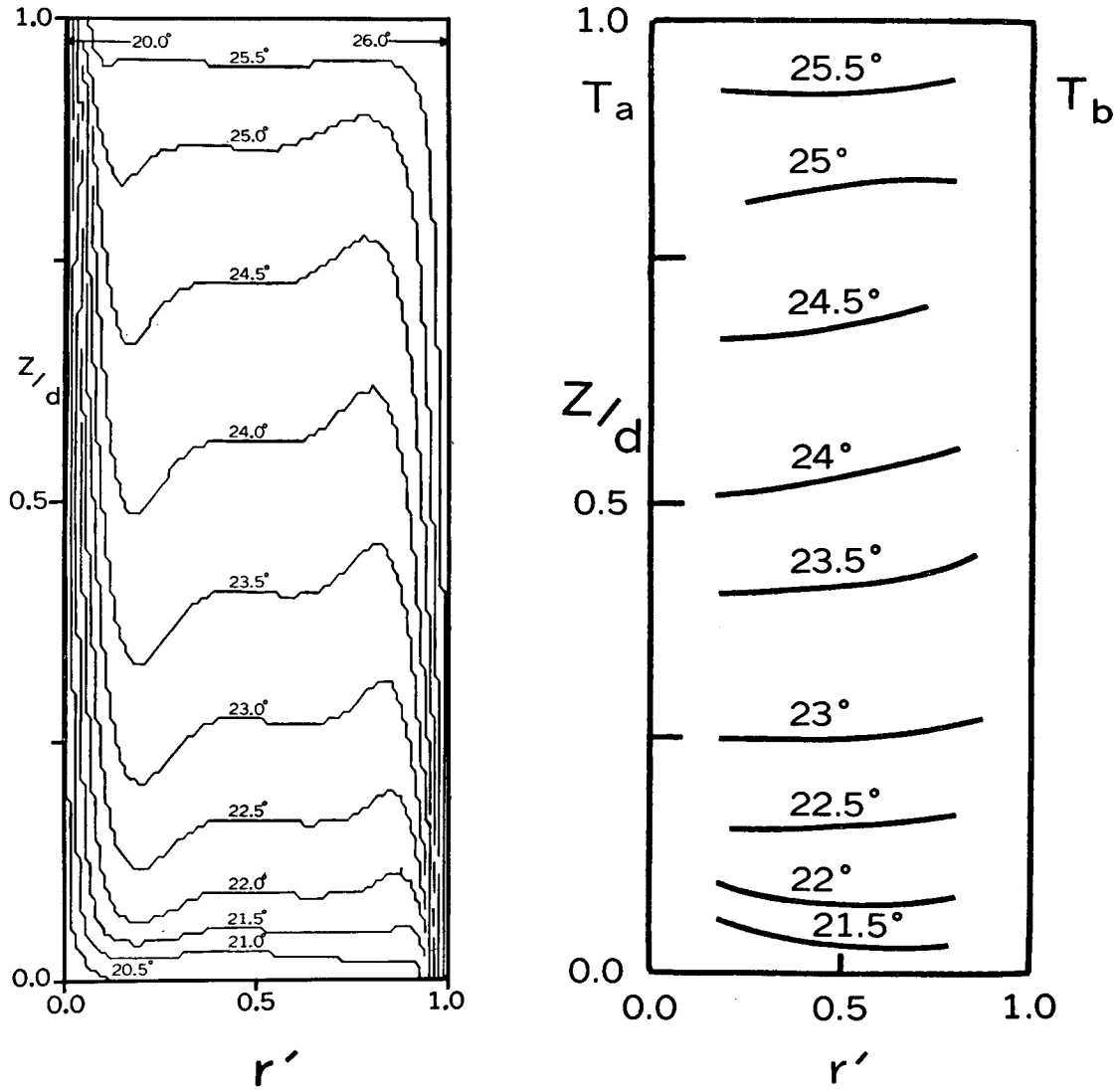

FIG. 2. A comparison of temperature distributions between the calculated values on the left and those observed by Bowden and Eden (1965). The dimensionless radial coordinate, $r' \equiv (r-a)/(b-a)$, measures distance from the inner (cold) cylinder at the left of each diagram, to the outer cylinder.

stream function occurs near the outer cylinder and the maximum vorticity near the inner cylinder, both close to the $z/d=0.5$ height. The vorticity field displays well formed boundary layers on both cylinder walls, but has nothing comparable on the horizontal surfaces; away from the side walls the vorticity is negligible. Elder (1965) has examined the flow between two heated vertical plates, a system equivalent to an annulus of zero curvature. His detailed observations of the temperature and flow fields display precisely the same features as those of the computations of case A1.

The flow in case A1 can be considered as being essentially the interaction of two thermal boundary layers, one on the outer cylinder, the other on the inner cylinder. The flow on each cylinder wall resembles that near an isolated vertical plate except that the influence of the one layer inhibits the vertical extent of the other layer beyond the central region $z/d=0.5$. In an isolated thermal boundary layer on a hot wall, the flow would be upward together with an entrainment of fluid from the interior. However, in the annulus, the entrainment requirements cannot be satisfied for both walls in the same way as they could be for isolated walls. The mutual interaction of the layers limits entrainment into the hot (outer) layer to the lower half of the wall and into the cold layer only in the upper half, making the central region the point of maximum growth of the boundary layers. The entrainment into one layer from the other occurs more or less by horizontal flow, as the streamlines of Fig. 4(A1) indicate. Furthermore, this cross flow tends to be isothermal and is associated with the horizontal configuration of the isotherms near the $r=(a+b)/2$ plane.

Analysis of the individual terms forming the temperature field [Fig. 5(case A1)] confirms that the interior flow is isothermal, conductive transfer being negligible except in the boundary layers. The constituent terms of the vorticity equation (Fig. 6) indicate that a balancing of viscous and buoyancy forces produces the motion of all regions, the nonlinear terms being negligible. With a knowledge of this balance, consider the motion in the central core region. From the fact that the mutual interaction of the boundary layers inhibits entrainment and further growth of the layers, we expect the radial velocity v to be zero. The computations show this to be so. Then the continuity equation gives a vertical velocity $w=w(r)$ and the steady state equations take the form:

$$\zeta=-w_r, \tag{1}$$

$$\beta g\Delta T\theta_r=\nu(1/r(r\zeta)_r)_r, \tag{2}$$

$$w\theta_r=\kappa[\theta_{zz}+1/r(r\theta_r)_r], \tag{3}$$

for the central core. Eliminating the r derivatives of θ yields the equation

$$w\theta_z-\kappa\theta_{zz}=-\frac{\kappa\nu}{\beta g\Delta T}\left[\left(\frac{1}{r}(rw_r)_r\right)_{rr}\right], \tag{4}$$

which on being differentiated throughout by z gives $\theta_{zz}=0$. This argument, derived from Elder (1965), indicates that the central region of the fluid has a linear temperature profile, a feature already noted.

3. Solutions of a set of flows with a rigid surface

To understand the annulus flow system, we have to know what types of flow are possible and under which physical processes the types exist, that is, whether the diffusion or convection processes predominate for a given flow type. The series of five rigid surface flow solutions to be described, provided a sufficient coverage of the whole range of physical processes. The cases will be examined separately, starting with flows controlled by diffusion and proceeding toward more convective flows, and then their relative implications will be discussed.

Case D1. Conduction and viscous forces essentially determine the first flow that we consider, namely D1. Weak heating and strong rotation rates (see Table 1) place this flow within the lower symmetric regime.

The stream function contours [Fig. 4 (case D1)] form a meridional flow composed of a large direct (Hadley) cell together with a smaller secondary cell system. The latter system is made up of 2 cells, each associated with one of the boundary layers on the inner and outer cylinders. Both cells penetrate the interior of the fluid where a very weak intermediate third cell also exists. The secondary cells, or countercurrents as Robinson (1959) terms them, strengthen the mass transport near the wall but weaken it elsewhere. The maximum value of the stream function arises near the center the of boundary layer on the outer cylinder, this being the position of strongest vertical flow. The flow field is asymmetric in the vertical plane.

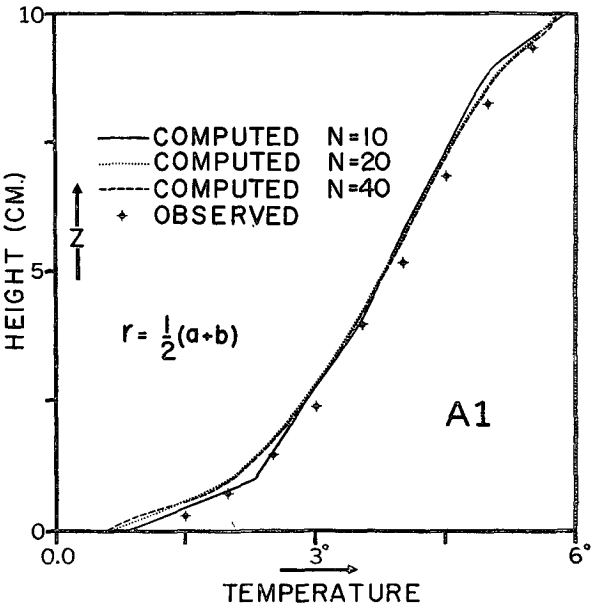

FIG. 3. A comparison for flow A1 of the vertical temperature distributions at $r'=\frac{1}{2}$, as given by the observations of Bowden and Eden (1965) and by the computations with 10, 20 and 40 grid spaces (N) in each dimension. Note that computational-observational disagreement is independent of resolution.

The temperature field deviates only slightly from the conductive solution. The effect of motion upon the temperature field is most apparent in a vertical temperature profile (Fig. 8). In the radial profiles (Fig. 9), the temperature field is linear at $z/d=0.25$ but at $z/d=0.75$ the solution is not so purely conductive. The temperature component balance [Fig. 5(case D1)] exhibits a wave number 2 variation in the convective terms at $z/d=\frac{1}{4}$. This reflects the large countercurrent contributions to the heat transport.

The zonal flow consists of westerly flow in the upper half of the annulus and easterly flow in the lower half. The line of separation, $u=0$, inclines up toward the inner (cold) cylinder with its mean height slightly below $z/d=\frac{1}{2}$. The maximum westerly just exceeds the maximum easterly, but both occur off-center, nearer the inner cylinder at a nondimensional distance of $r'=\frac{1}{4}$. Small but identifiable Ekman layers exist on the lid and base.

A typical balance of vorticity equation components [Fig. 6(case D1)] reveals that the interior of the fluid is essentially in a geostrophic balance despite the viscous-conductive nature of this lower symmetric regime flow. However, the extent of the geostrophic region is small compared to similar regions in other flows. The vorticity boundary layers exist under a balance of friction and buoyancy forces. The contribution of convective transport to the vorticity balance and zonal velocity balance (Fig. 7) is negligible. The components

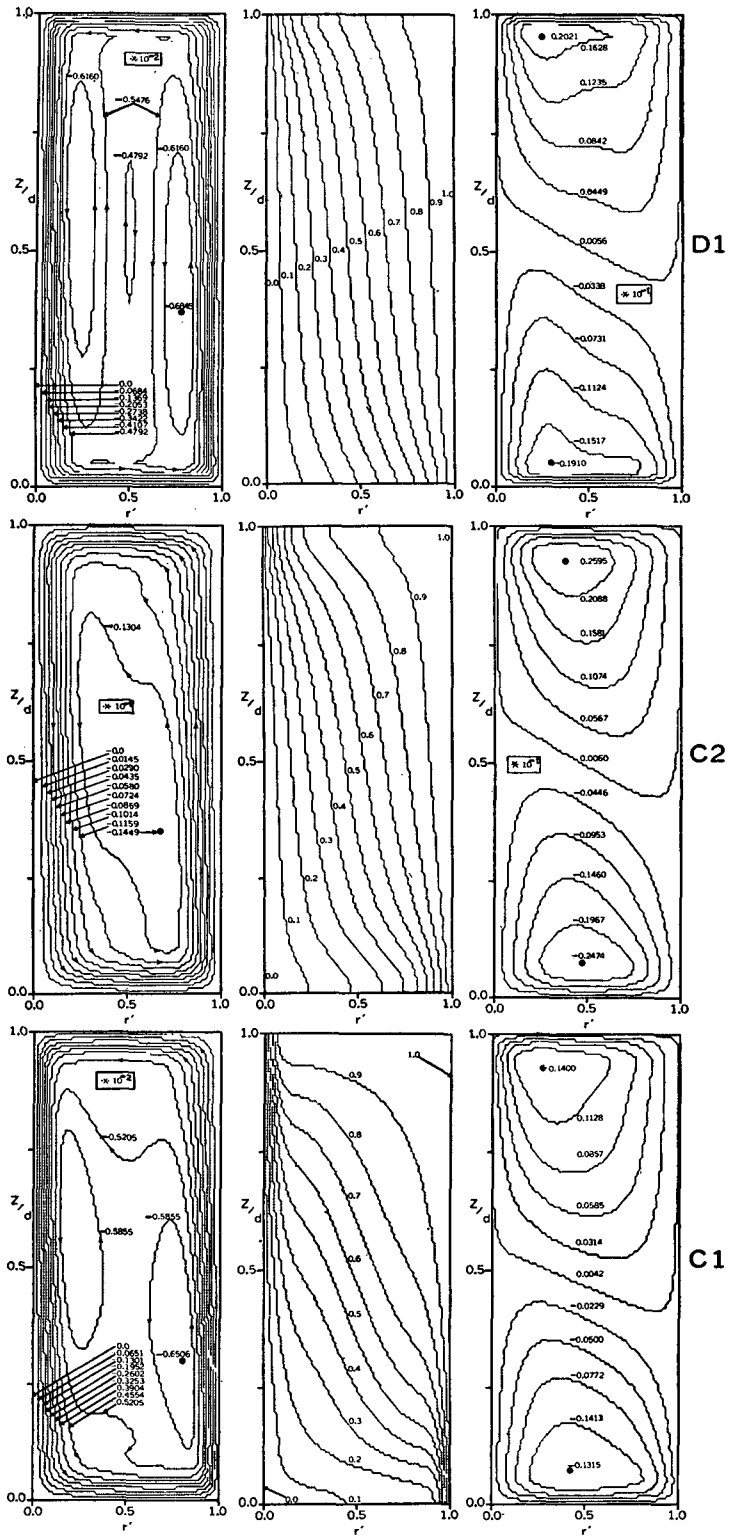

FIG. 4. Steady state contours of, from the left, stream function, normalized temperature and zonal velocity for flows D1, C2, C1, B1, A2 and A1 with a rigid upper surface (see Table 1). For flow A1 ($\Omega=0$), the vorticity contours replace the zonal isotachs. Streamline arrows indicate the meridional flow direction and a positive zonal velocity denotes a westerly flow, all in cm sec^{-1}. Extreme values of zonal velocity and stream function are marked.

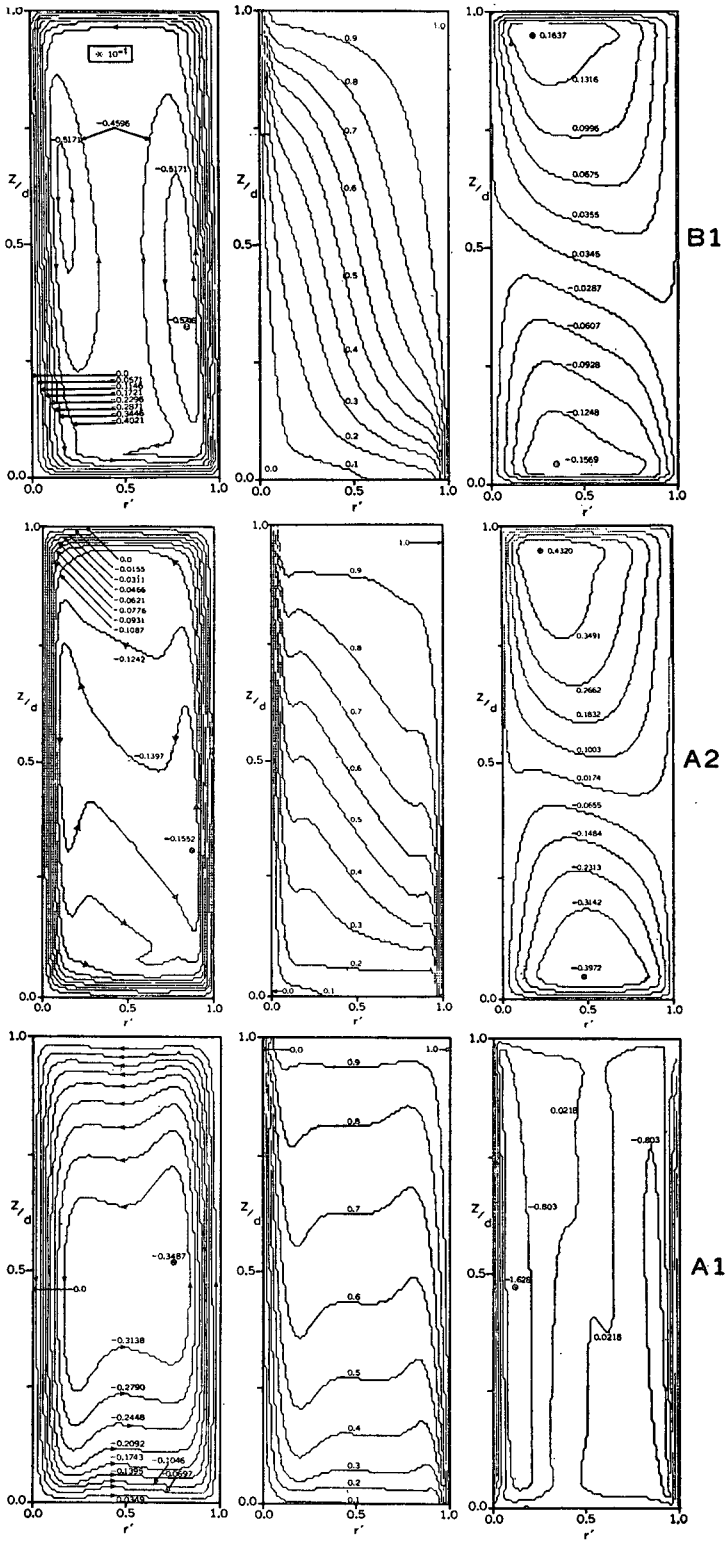

FIG. 4. (*Continued*).

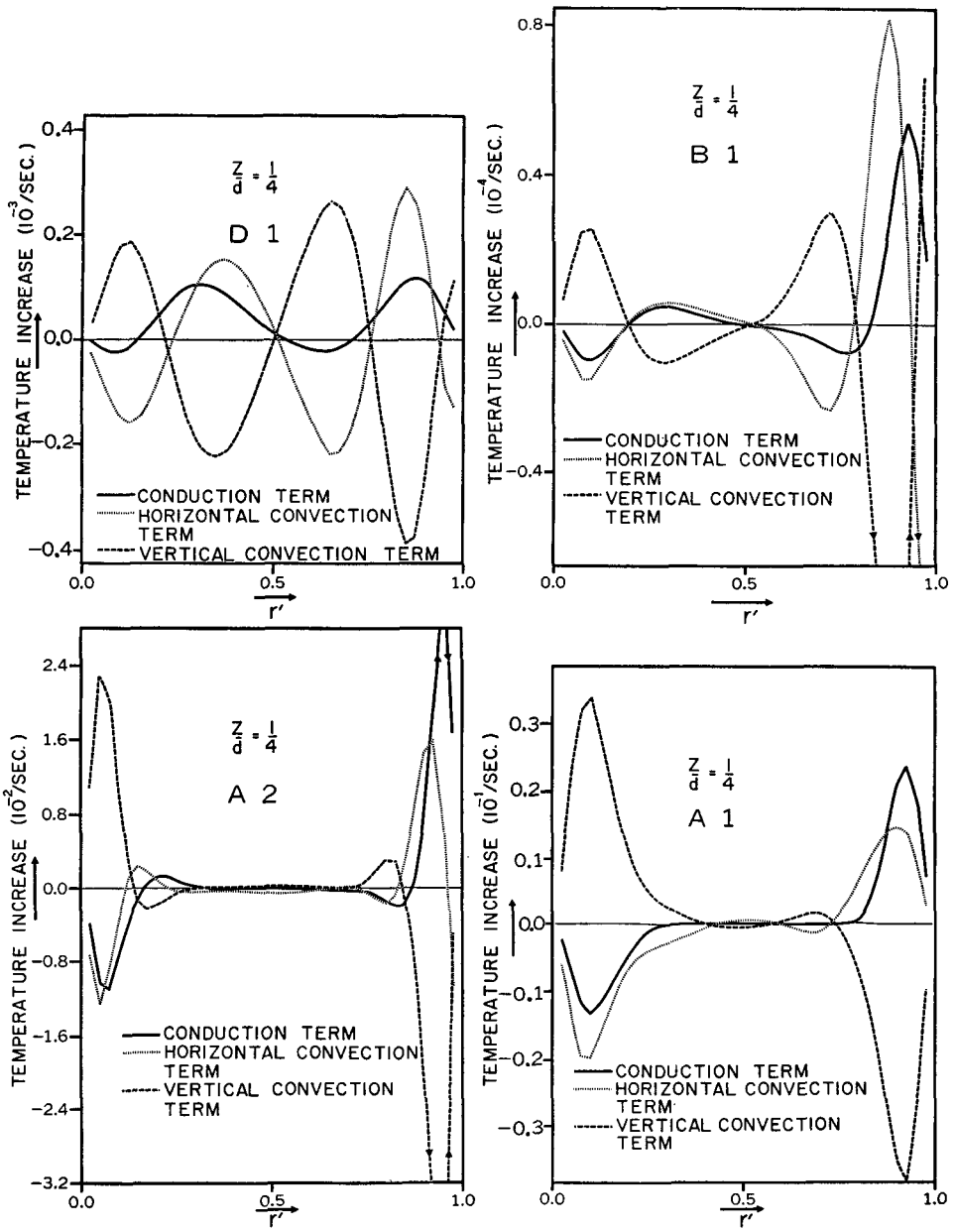

FIG. 5. Representative radial distributions of the components contributing to the balance of terms in the normalized temperature equation for 4 flows at height $z/d = \frac{1}{4}$. For the meaning of the terms consult Eq. (8) of Part 1.

of the zonal velocity equation exhibit a balance between the Coriolis term $-2\Omega v$ and the friction term $\nu\nabla^2 u$ throughout the fluid. This indicates that the meridional flow is mainly frictionally driven.

Case C2. A low rotation rate places case C2 higher up on the convective scale compared to flow D1, and the flow lies in the mid-symmetrical regime.

The meridional flow forms a direct cell and occupies broad boundary layer regions of the fluid as a consequence of the low rotation rate. The structure of the interior secondary flow is less pronounced than that of other cases. The customary two cells, such as are present in D1, have fused into one for the flow of C2.

The increasing convective influence is clearly marked in the temperature field as shown in Figs. 4, 8 and 9. Although the conduction solution predominates in the central core of the fluid, the isotherms are convected by the meridional flow in the base and lid regions where there is a marked concentration of the isotherms. A Nusselt number of 1.40 for this flow indicates the effect of convective heat transport upon the basic conduction Nusselt number of 1.0. The Nusselt number of 1.15

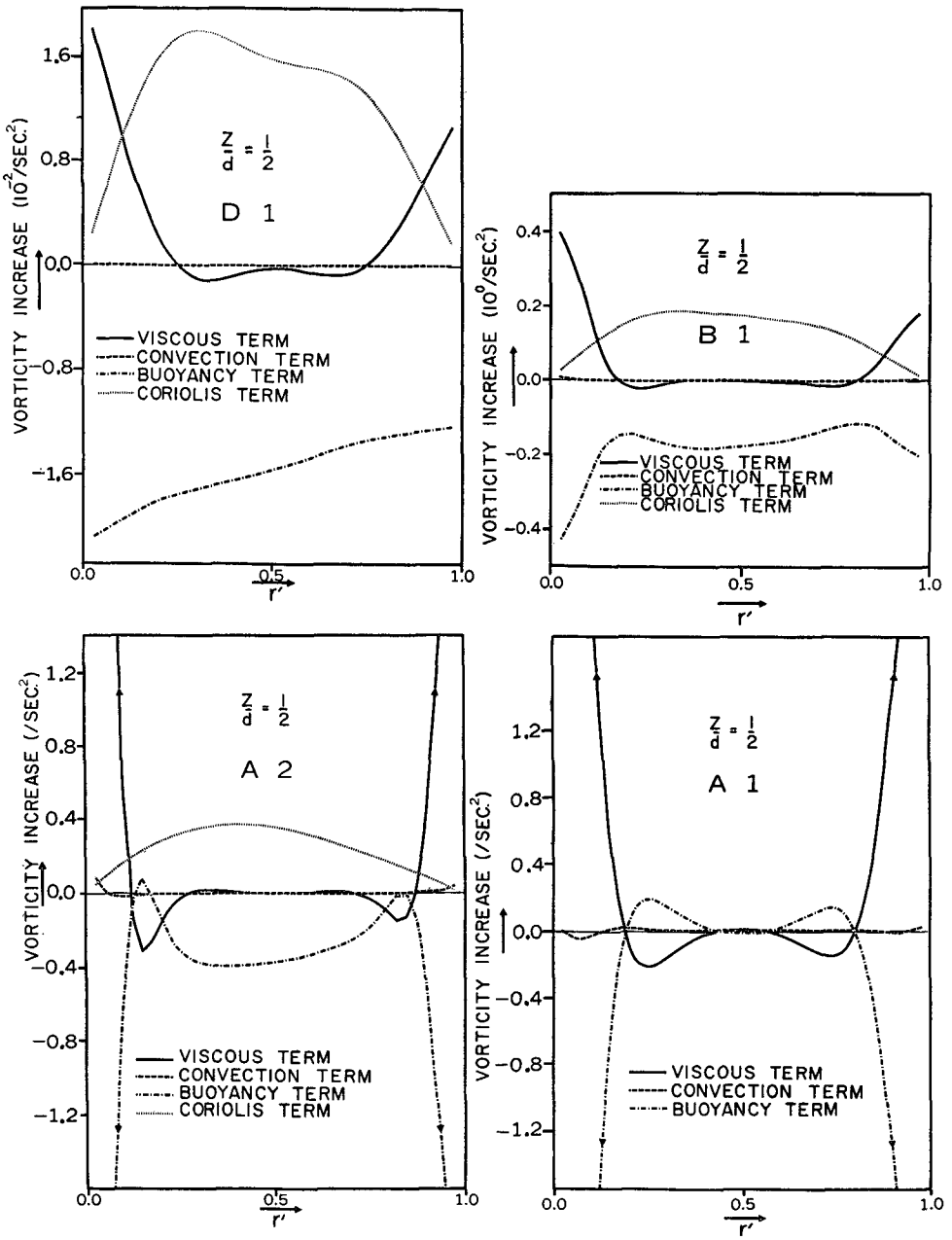

FIG. 6. Representative radial distributions of the components contributing to the balance of terms in the vorticity equation (7) of Part 1, for various flows at mid-height. The geostrophic nature and extent of the interior are illustrated.

for the previous case, D1, indicates the essentially conductive nature of that flow. The Nusselt number determines quantitatively the position of the flow on the convective scale.

The zonal velocity contours of C2 display a more rounded shape and have larger magnitudes than those of D1. Furthermore, the extreme values, both occuring near $r' = \frac{1}{2}$, are more centrally located. The deep Ekman layers are in keeping with the low rotation rate.

Case C1. The flow of case C1 is made predominately convective by a temperature difference that is relatively large when compared to those of flows dominated by conduction.

The stream functions of cases C1 and D1 are of similar magnitude. Thus, as the flow of case C1 has the higher temperature difference ΔT and the lower rotation rate Ω, these parameters must produce opposite effects, i.e., the temperature gradient induces and the rotation inhibits meridional mass transfer. Although of convective origin, the flow of C1 has the same basic structure as the conductive flow D1; only the lesser details differ. In particular, the boundary

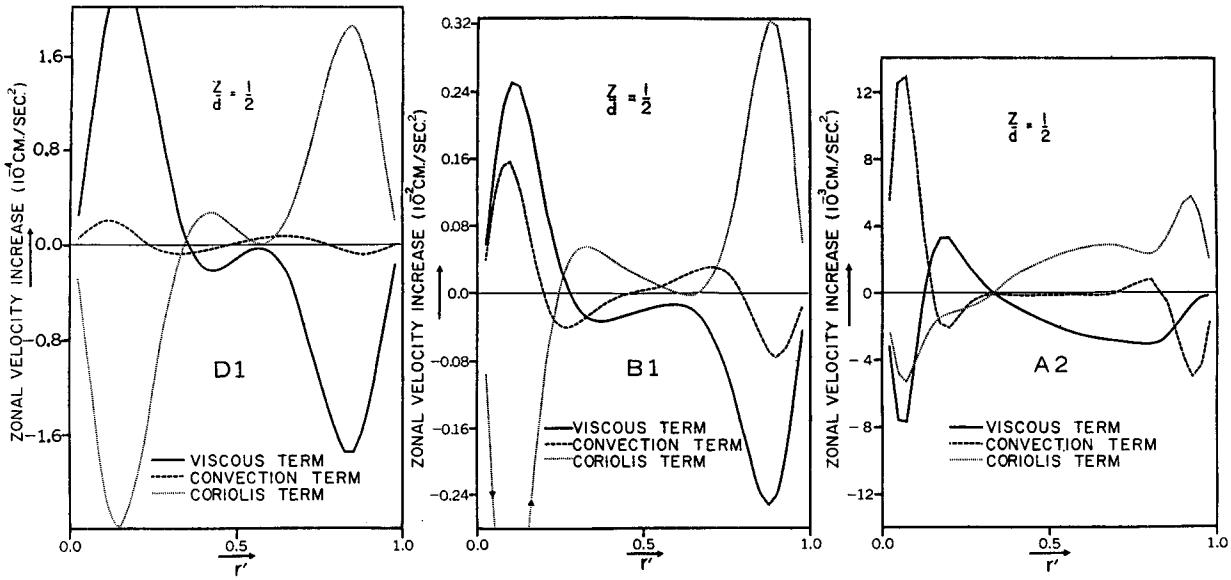

FIG. 7. Representative radial distributions of the components contributing to the balance of terms in the zonal velocity equation (9) of Part 1, for various flows at height $z/d=\frac{1}{2}$.

layer streamlines are more rounded at the corners, suggesting that the horizontal and vertical boundary layers interact more strongly in convective flows. The momentum boundary layers broaden out as the fluid progresses up the outer cylinder and down the inner cylinder, in keeping with the localized concentration of the isotherms into definitive thermal boundary layers. Two secondary cells exist again, this time in a strong, precise form and exhibiting asymmetry about the line $z/d=\frac{1}{2}$. This last feature is associated with the asymmetric structure of the thermal boundary layers.

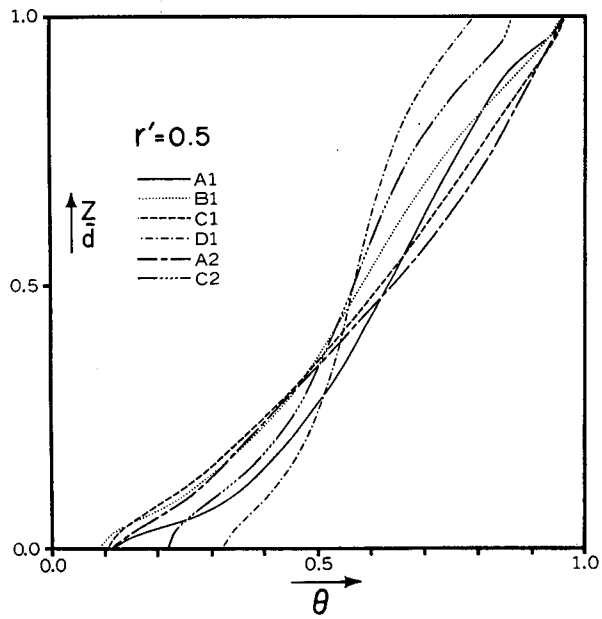

FIG. 8. Profiles of the vertical distribution of normalized temperature at $z/d=\frac{1}{2}$ for the rigid surface flows.

Brevity of extent distinguishes the thermal boundary layers, for both layers form along only one-fourth of each cylinder. Temperature profiles [Fig. 9(case C1)] show the existence of separate interior and boundary layer regions in the radial direction. The interior isotherms display a determined linearity in their general sloping up toward the inner cylinder. A large region of fluid, near the lid, lies at almost constant temperature between the 0.9 and 1.0 isotherms.

As in all other rigid surface flows, the zonal velocity has extreme values of almost equal magnitude. However, the maximum westerly occurs near $r'=\frac{1}{4}$ while the easterly maximum is positioned near $r'=\frac{1}{2}$.

Case B1. The external parameters place this flow within what observations indicate is the wave regime of free surface flows. However, the presence of a lid and absence of a stability criterion for viscous-conductive flows makes it uncertain whether flow B1 lies in the wave regime or not. All that can be said is that a steady state axisymmetric solution (Fig. 4) exists for the parameter values of B1.

The parameters of case B1 resemble those of D1 in all respects apart from the temperature difference which is 10 times greater for flow B1. In direct consequence, the meridional velocities are approximately 10 times greater for B1 than D1. All the flow features are essentially the same as those of C1 so that they require no separate description. Although the same types of physical processes are involved in flows B1 and D1 as shown in Figs. 5, 6 and 7, i.e., both flows have geostrophically balanced interior flows, the extent of such similar regions varies from flow to flow.

Case A2. The final Case, A2, in this comparative series lies in the upper symmetric regime because of its relatively large temperature difference. This flow also com-

pares with the free surface flows of the same regime considered in Part 1. The superiority of the rigid surface system as a mass and heat transporter is made evident by such a comparison.

The secondary cell structure of case A2 differs from those of the other flows. As a type, it falls between that of the convective case A1 ($\Omega=0$) and that of the general pattern, such as occurs in B1. Although two small individual wall cells may exist, a single cell system is the predominant feature of the secondary flow.

The isotherm contours contain the most interesting aspect of the A2 flow, namely the vanishing of the radial temperature gradient θ_r (Figs. 4 and 9). The S-shaped contours, containing this inflection, form separate regions between the boundary layers and the interior proper. The viscous boundary layer being broader than the thermal boundary layer frictionally drags the interior fluid along, thereby producing the isotherm inflections. A composite diagram of stream function and temperature contours (Fig. 10) indicates that the secondary cell system augments or coincides with the temperature inflections; the essentially isothermal nature of the interior flow is also apparent. The S-shape of the isotherms means that heat is being conducted in toward the flex point from both sides to compensate for excessive convection.

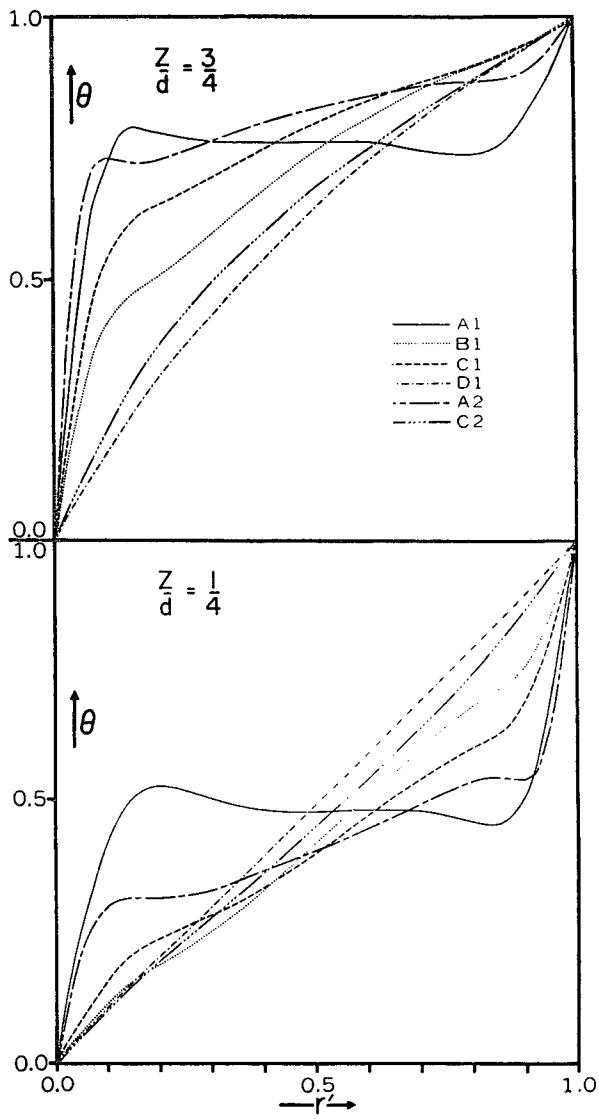

FIG. 9. Profiles of the radial distribution of temperature for the rigid surface flows at levels $z/d=\frac{1}{4}$ and $\frac{3}{4}$. Gradients lie between that of the conductive flow D1 and the nonrotating convective flow A1.

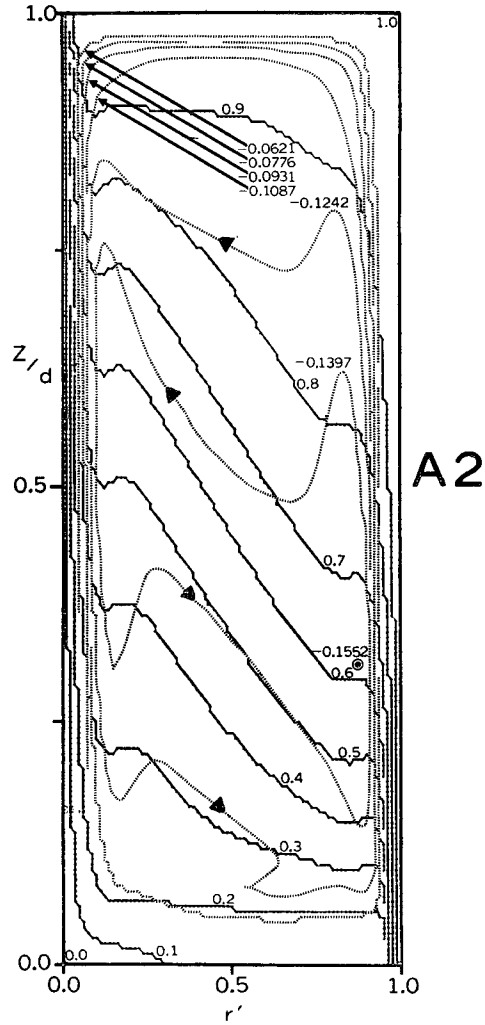

FIG. 10. A composite of the isotherms and interior streamlines of flow A2 illustrating the isothermal nature of the interior flow and the association of thermal and viscous boundary layers.

The vorticity component balance shown in Fig. 6(case A2) also reflects the existence of three regions. Apart from a normal ($\Omega\neq0$) interior region in a buoyancy-Coriolis (geostrophic) balance and boundary layers in buoyancy-viscous balance, there is one area between these two regions where the Coriolis and viscous terms of the vorticity equation balance.

TABLE 2. Nusselt numbers and integration periods.

Case	Nu(a)	Nu(b)	Nū tendency	Approximate steady state time (a) Sec	(b) Revolutions
D1	1.15	1.16	1.15	500	90
C2	1.36	1.42	1.40	1000	60
B1	3.52	3.68	3.60	500	90
C1	3.94	3.90	3.93	1000	80
A2	8.24	8.40	8.32	400	60
A1	6.33	6.37	6.35	600	—
A3	7.98	8.30	8.14	300	60
B2	5.00	5.35	5.18	330	110

a. Comparison of flow properties

1. Component balances.

All the flows which we have considered ($\Omega \neq 0$) display the same basic east-west pattern of zonal flow in conically shaped regions, separated just below the $z' = \frac{1}{2}$ level by the $u = 0$ contour. Typical distributions of the component terms of the steady state zonal velocity equation shown in Fig. 7, have interior regions that are always in a Coriolis-zonal velocity friction term balance. However, the size of these interior regions diminishes for the strongly viscous flows of the lower symmetric regime. The term expressing the meridional convection of zonal velocity makes little contribution to the balance of the interior but in upper symmetric regime cases, such as A2, it constitutes a large part of the friction layer balance, particularly on the inner cylinder. Generally, however, the zonal velocity boundary layers are in a Coriolis-zonal velocity friction balance.

The component balances of the temperature equation (Fig. 5) reveal the comparative rôle of conduction in the various flows. In the lower symmetric regime, the flow D1 transports heat by convection with conduction playing an equally large role throughout the fluid. Significant conduction contributions are confined to well defined thermal boundary layers in other flows. Furthermore, in the upper symmetric regime, there appears to be little heat transport by either convection or conduction in the interior. The thermal boundary layers of Case A1 ($\Omega = 0$) are uniformly formed and radial convection and conduction match convection in the vertical.

2. Heat transfer.

As it is not practical to present all the energy integral diagrams, we restrict consideration to the Nusselt number integrals. The annulus is essentially a heat transporting mechanism and the Nusselt number forms the most tangible measure of the dependence of the system upon the parameters. The values of the parameters π_4 and π_5 have already been seen to determine the type of flow produced. The values of the Nusselt numbers of the various solutions are presented in Table 2.

For a non-rotating annulus, the Nusselt number has been observed to be proportional to $(\Delta T)^{\frac{1}{4}}$ [e.g., Bowden and Eden (1965)]. Using this fact as a guide, a plot of $\text{Nū}(\Delta T)^{-\frac{1}{4}}$ against the Rossby number π_4 for the 5 rigid lid flows yields a straight line on the logarithmic scale of Fig. 11. As the only parameters varied in the investigation are ΔT and Ω, the line has the equation

$$\text{Nū} = 2.6\frac{\Delta T^{0.47}}{\Omega^{0.44}} \equiv 2.6\left(\frac{\Delta T}{\Omega}\right)^{\frac{1}{2}}\left(\frac{\Omega^2}{\Delta T}\right)^{0.03}. \qquad (5)$$

This relationship cannot be regarded as anything more than a convenient expression as it is not based on any physical deductions. In the upper symmetric regime the second parenthesis in (5) is equal to unity so that Nū behaves as $(\Delta T/\Omega)^{\frac{1}{2}}$.

For the two free surface experiments Nū behaves as Ω^{-1}, ΔT being constant for these experiments. The functioning of annulus heat transport in accordance with $(\Delta T/\Omega)^{\frac{1}{2}}$ for rigid surface flows and with Ω^{-1} for free surface flows is only a crude indication of the fluid behavior in view of the small number of solutions from which the relationships were derived. If the relations are meaningful, they infer that free surface flow is inhibited by rotation to double the power by which the rigid surface flow is inhibited.

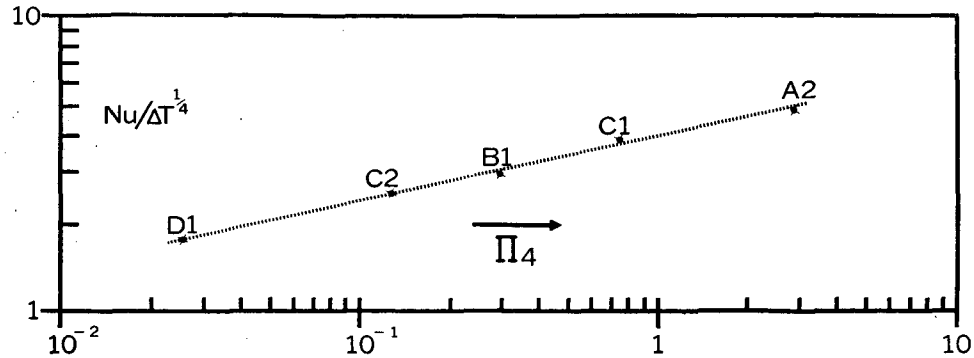

FIG. 11. The logarithmic variation of Nusselt number Nū with the Rossby number, $\pi_4 = (g\beta d\Delta T)/[\Omega^2(b-a)^2]$, for 5 fixed surface flows ($\Omega \neq 0$).

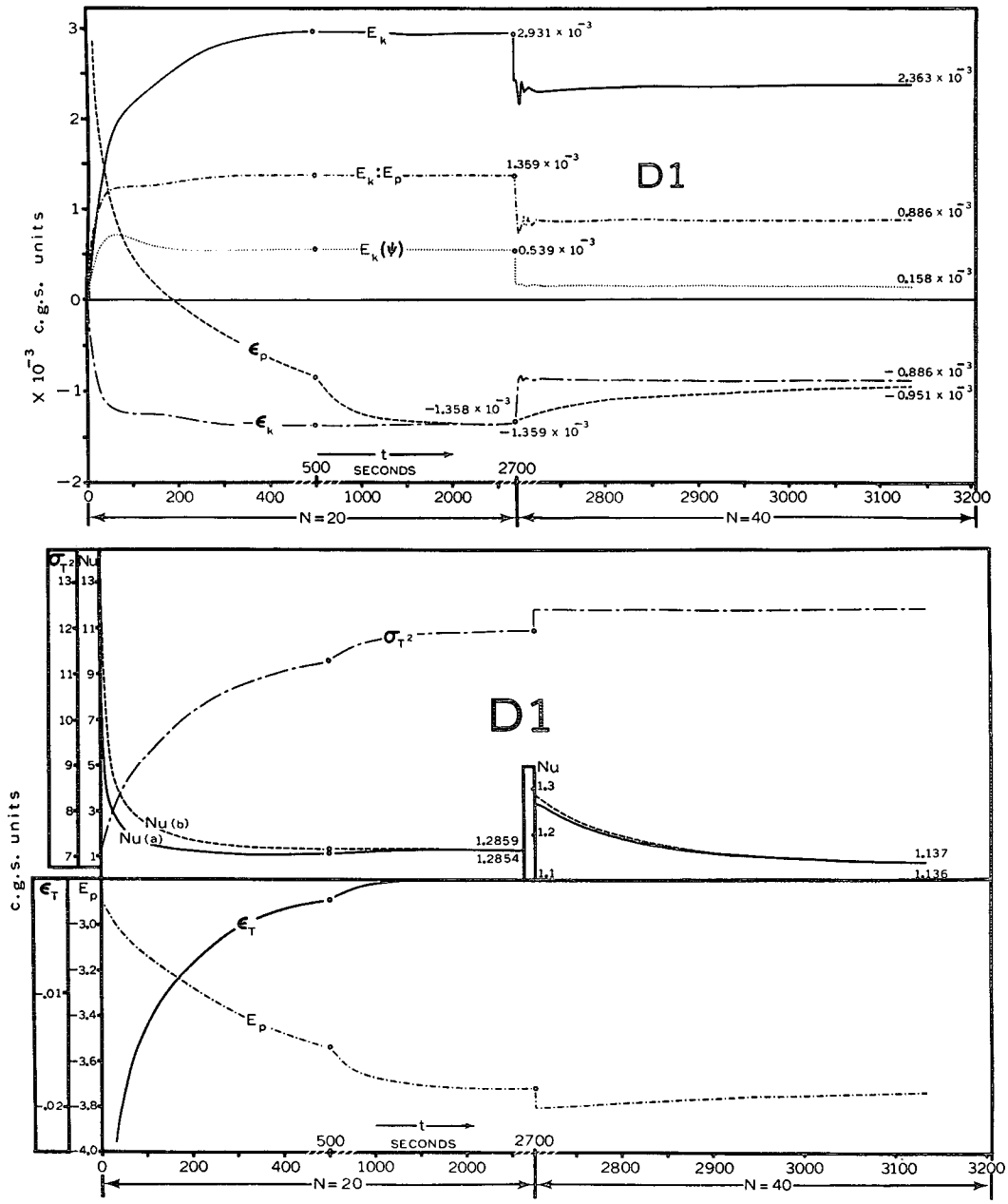

FIG. 12 a, b. The integral quantities (see Part 1) of D1 are shown as functions of time. The time scale is composed of 3 separate stages and the grid resolution is doubled at 2700 sec.

3. Steady state requirements.

The flows considered require the equivalent in time of 60 to 100 revolutions of the annulus to achieve a steady state as shown in Table 2. In terms of real time, the flows of the lower symmetric regime take the longest time to reach steadiness and the upper regime flows take the shortest. The two free surface flows require roughly the same amount of time despite the difference in rotation rates.

Fig. 12 shows what happens when the solution with a particular grid is used as the initial state for an integration with double the resolution. The primary solution for the 20×20 grid is reasonably steady after 500 sec, but the integration is further developed to 2700 sec, by which time diffusive mechanisms have produced Nusselt numbers differing only in the fifth digit. At this time, the 20×20 solution is linearly interpolated onto a 40×40 grid to commence integration with the increased resolution. The kinetic integrals all jump in magnitude but become constant again after 20 sec. The temperature integrals, however, take about 500 sec to return to steadiness; this is the same length of time

as the initial grid integration required so there is little advantage to be derived from performing integrations in the above manner.

4. Discussion and conclusions

The resemblance of the cases considered to the conductive type D1 and to the convective type A1($\Omega=0$) indicates that flows may be regarded as being combinations of these two basic types. The radial temperature distributions support this approach because the profiles (Fig. 9) progress in structure from the linear profile of D1 to the S-shaped profile of A1. Thus, the inflections that occur in the temperature contours near the boundary layers in case A2 are essentially a feature of the non-rotating flow A1. The meridional flow structures vary from the large two cell secondary flows of D1, through diverse cell sizes, to the single cell interior structure of A1 (and A2).

The mutual interaction of the thermal boundary layers primarily determines the temperature field of a particular flow. The requirement that the isotherms of one thermal boundary layer join up with those of the other layer limits the extent of the layers along the walls and produces an interior distribution; case A1 with its zero rotation demonstrates this. The rotation of the annulus effects a sloping of the interior contours and reduces the size of the thermal boundary layers.

The lack of extensive observation allows us to make only a qualitative examination of the solutions. The data of Bowden and Eden agree with the sloping of isotherms by rotation and with the composition of the zonal velocity field. The observed zonal velocity extrema are more centrally located than those of the calculations, but the positioning of the $u=0$ isotach separating east-west flow is the same.

The only theoretical work on flow structure that can be applied to the solutions is the analysis of Robinson (1959). His theory is valid for flows with a temperature field determined predominately by conduction. Case D1 satisfies this criterion and is open to comparison, particularly as it lies within the convergence requirements of the analysis. Theory predicts the direct meridional circulation and two symmetric secondary cells associated with the sidewall boundary layers. The limitations of the analysis could explain the symmetry of cells which are asymmetric in the numerical solution. Robinson's conclusion that the non-linear convection terms in the heat equation significantly control the development of the fields, while the non-linear momentum convection is negligible, has already been noted in Figs. 5 and 6 for case D1. The analytical result that at low rotation rates the boundary layer countercurrents may not be observable is true in case C2. The bow shaped distortion of the boundary layer streamlines, as obtained by Robinson, cannot be discerned in the numerical solutions.

According to theory, the sidewall countercurrents owe their existence to the interaction of the sidewall boundary layers and the rotationally constrained flow of the Ekman boundary layers on the base and lid. The mechanics of such a system are not obvious. The secondary cells are probably necessary to control the width of the sidewall layers so that they can flow smoothly into the Ekman layers.

Acknowledgments. The writer is indebted to Mr. S. Hellerman for use of his contouring program and to Miss M. B. Jackson and Mr. L. Reed for assistance in preparing the diagrams.

REFERENCES

Bowden, M., and H. F. Eden, 1965: Thermal convection in a rotating fluid annulus: temperature, heat flow and flow field observations in the upper symmetric regime. *J. Atmos. Sci.*, **22**, 185–195.

Elder, J. W., 1965: Laminar convection in a vertical slot. *J. Fluid Mech.*, **23**, 77–98.

Robinson, A. R., 1959: The symmetric state of a rotating fluid differentially heated in the horizontal. *J. Fluid Mech.*, **6**, 599–620.